


Advances in Global Change Research 69

Vincenzo Levizzani
Christopher Kidd · Dalia B. Kirschbaum
Christian D. Kummerow · Kenji Nakamura
F. Joseph Turk *Editors*



Satellite Precipitation Measurement

Volume 2

 Springer

Advances in Global Change Research

Volume 69

Series Editor

Markus Stoffel, Institute of Geological Sciences, University of Geneva, Geneva, Switzerland

Advisory Editors

Wolfgang Cramer, IMEP, Bâtiment Villemin, Europole de l'Arbois, Aix-en-Provence, France

Urs Luterbacher, University of Geneva, Geneva, Switzerland

F. Toth, International Institute for Applied Systems Analysis (IIASA), Laxanburg, Austria

More information about this series at <http://www.springer.com/series/5588>

Vincenzo Levizzani • Christopher Kidd
Dalia B. Kirschbaum • Christian D. Kummerow
Kenji Nakamura • F. Joseph Turk
Editors

Satellite Precipitation Measurement

Volume 2

 Springer

Editors

Vincenzo Levizzani
CNR-ISAC
Bologna, Italy

Dalia B. Kirschbaum
Code 617
NASA Goddard Space Flight Center
Greenbelt, MD, USA

Kenji Nakamura
Department of Economics on
Sustainability
Dokkyo University
Saitama, Japan

Christopher Kidd
Earth System Science Interdisciplinary Center
University of Maryland and NASA Goddard
Space Flight Center
Greenbelt, MD, USA

Christian D. Kummerow
Department of Atmospheric Science
Colorado State University
Fort Collins, CO, USA

F. Joseph Turk
Jet Propulsion Laboratory
California Institute of Technology
Pasadena, CA, USA

ISSN 1574-0919

ISSN 2215-1621 (electronic)

Advances in Global Change Research

ISBN 978-3-030-35797-9

ISBN 978-3-030-35798-6 (eBook)

<https://doi.org/10.1007/978-3-030-35798-6>

© Springer Nature Switzerland AG 2020

This work is subject to copyright. All rights are reserved by the Publisher, whether the whole or part of the material is concerned, specifically the rights of translation, reprinting, reuse of illustrations, recitation, broadcasting, reproduction on microfilms or in any other physical way, and transmission or information storage and retrieval, electronic adaptation, computer software, or by similar or dissimilar methodology now known or hereafter developed.

The use of general descriptive names, registered names, trademarks, service marks, etc. in this publication does not imply, even in the absence of a specific statement, that such names are exempt from the relevant protective laws and regulations and therefore free for general use.

The publisher, the authors, and the editors are safe to assume that the advice and information in this book are believed to be true and accurate at the date of publication. Neither the publisher nor the authors or the editors give a warranty, expressed or implied, with respect to the material contained herein or for any errors or omissions that may have been made. The publisher remains neutral with regard to jurisdictional claims in published maps and institutional affiliations.

Cover illustration: Courtesy of NASA

This Springer imprint is published by the registered company Springer Nature Switzerland AG.
The registered company address is: Gewerbestrasse 11, 6330 Cham, Switzerland

*Sognatore è un uomo con i piedi fortemente
appoggiati sulle nuvole**

Ennio Flaiano (1910–1972)

**Dreamer is a man with his feet firmly resting
on the clouds*

In memory of
Arthur Y. Hou (1947–2013)

Preface

This book is published 13 years after the book *Measuring Precipitation from Space: EURAINSAT and the Future* (V. Levizzani, P. Bauer, and F. J. Turk, Eds., Springer, ISBN 978-1-4020-5835-6), but it is not a revised edition of the previous. It is a new book that aims to construct a quasi-complete picture of the science and applications of satellite-derived precipitation measurements at the present time.

The book comes out at the end of a very exciting era of precipitation measurements from space. The Tropical Rainfall Measuring Mission (TRMM), launched in November 1997, ended its long life in space in April 2015 providing an unprecedented 17-year-long dataset of tropical precipitation and lightning. The Global Precipitation Measurement (GPM) mission, launched in February 2014, is now in space as TRMM's natural successor with a more global perspective that extends precipitation radar observations to the Arctic and Antarctic circles. At the same time, the CloudSat mission, launched in April 2006, is in its 13th year in space and focuses on cloud structure, which is essential for improving precipitation retrievals. These are just a few examples of precipitation-oriented missions that continuously provide data from geostationary and low Earth orbits in a truly cooperative effort worldwide. This effort involves many agencies and a broad range of countries who collaborate in a genuine way to observe global precipitation.

It is by realizing the significance of this historical moment and the need to think about what is important for the future that the community joined in the effort of writing a book with the goal of serving the precipitation community itself, the scholars, the students, the stakeholders, the end users, and all the readers interested in knowing the progress of satellite precipitation studies. The most recent achievements in precipitation monitoring from space drive us into the future of measuring not only heavy rainfall but less intense rainfall, snowfall, and even hailfall. Such a scientific framework would not have even been conceivable 13 years ago and is only possible thanks to the relentless effort of the worldwide space and precipitation communities.

Naturally, we realize that at the time of the printing of this book, the field will already have made advances and thus part of the material may already be a bit

outdated. However, in this era of rapidly evolving technological developments, sensors that take years to design, build, and launch are already considered old. This is particularly true nowadays when the progress in approaching new scientific challenges is particularly fast.

Since 2007, science has made substantial progresses toward transforming satellite rainfall “estimates” into accurate “measurements” and producing operational rainfall products readily available for a wide field of applications ranging from climate research and numerical weather prediction to hydrology, agriculture, health, civil protection, and much more. Satellite-derived precipitation products are now being considered as a valuable tool for a number of applications that benefit society and save lives. This is perhaps the most important achievement of all.

This book represents a significant effort, and each author has provided high-quality material in the topics of current and future mission contributions, observations of precipitation using the suite of precipitation satellites, retrieval techniques, validation, and applications. The result is a book that not only photographs the state of the art of the discipline but also projects it into the future.

Bologna, Italy
Greenbelt, MD, USA
Greenbelt, MD, USA
Fort Collins, CO, USA
Saitama, Japan
Pasadena, CA, USA
9 March 2020

Vincenzo Levizzani
Christopher Kidd
Dalia B. Kirschbaum
Christian D. Kummerow
Kenji Nakamura
F. Joseph Turk

Acknowledgments

The first acknowledgment goes to Springer Nature for asking us to start this project and for being very patient with us for the considerable amount of time it took to put the material together.

All the colleagues who spent their precious time contributing their ideas and results deserve special gratitude. They are all very busy scientists, and this is why their contribution is particularly valuable. We deem the book to be a first-hand image of the achievements of the whole community at this time while also providing an important glimpse into future developments.

Then we feel that we need to thank the readers who have already made the previous 2007 Springer book a success, thus de facto making it possible to start writing the new one. We hope you will get from this new book even more inspiration than you got from its predecessor. While some concepts and details will surely become outdated as time goes by, it is our hope that the material contained herein is sufficiently broad that it will always serve as a springboard to understand and put into context the latest research and findings.

It would be almost impossible to thank all the people and organizations behind this effort. You realize this simple truth by looking at the list of contributors and seeing the very long list of institutes, research organizations, university departments, and operational agencies that allowed their members to spend a substantial amount of time writing and correcting the chapters of the book. We thank, in particular, our home institutions that were very supportive in understanding the importance of our work for the community: CNR, Colorado State University, Dokkyo University, JPL-Caltech, NASA, and University of Maryland.

It is very important to remember all the colleagues who are no longer with us and who worked very hard until the last minute providing an essential contribution. This book is dedicated to the memory of a friend of all of us, Arthur Y. Hou (1947–2013). Arthur was not only the US Project Scientist of the Global Precipitation Measurement (GPM) mission, he was a man of a truly global vision who now is in place with the GPM constellation. More than that, he made great efforts to establish an international science cooperation through his gentle and unique way of approaching

each one of us. Other colleagues left us in recent times, and we want to honor them as well: David (Dave) H. Staelin (1938–2011), David I. F. Grimes (1951–2011), and James (Jim) A. Weinman (1930–2012). They all left us much too soon, and we miss them, but their work is here to testify to their essential contribution to the advancement of science and to meet the needs of mankind.

Two major international organizations gave us the opportunity to work together with a global strategy for the future: the International Precipitation Working Group (IPWG) and the World Meteorological Organization (WMO).

The senior editor (Vincenzo Levizzani) would like to recognize the ceaseless work of his coeditors in effectively putting together the material of their respective sections: F. Joseph (Joe) Turk for Section 1, Christian (Chris) D. Kummerow for Sections 2 and 3, Christopher (Chris) Kidd for Section 4, Kenji Nakamura for Section 5, and Dalia B. Kirschbaum for Section 6. Their commitment and competence largely influenced the quality level of this book.

Finally, our families are part of the project through their understanding and their moral and practical support. Without them, the writing of this book would have never even started.

Bologna, Italy
 Greenbelt, MD, USA
 Greenbelt, MD, USA
 Fort Collins, CO, USA
 Saitama, Japan
 Pasadena, CA, USA
 9 March 2020

Vincenzo Levizzani
 Christopher Kidd
 Dalia B. Kirschbaum
 Christian D. Kummerow
 Kenji Nakamura
 F. Joseph Turk

Contents of Volume 2

Part IV Validation

25	The IPWG Satellite Precipitation Validation Effort	453
	Christopher Kidd, Shoichi Shige, Daniel Vila, Elena Tarnavsky, Munehisa K. Yamamoto, Viviana Maggioni, and Bathobile Maseko	
26	The GPM Ground Validation Program	471
	Walter A. Petersen, Pierre-Emmanuel Kirstetter, Jianxin Wang, David B. Wolff, and Ali Tokay	
27	The GPM DPR Validation Program	503
	Riko Oki, Toshio Iguchi, and Kenji Nakamura	
28	Error and Uncertainty Characterization	515
	Christian Massari and Viviana Maggioni	
29	Multiscale Evaluation of Satellite Precipitation Products: Effective Resolution of IMERG	533
	Clément Guilloteau and Efi Foufoula-Georgiou	
30	Remote Sensing of Orographic Precipitation	559
	Ana P. Barros and Malarvizhi Arulraj	
31	Integrated Multi-satellite Evaluation for the Global Precipitation Measurement: Impact of Precipitation Types on Spaceborne Precipitation Estimation	583
	Pierre-Emmanuel Kirstetter, Walter A. Petersen, Christian D. Kummerow, and David B. Wolff	
32	Hydrologic Validation and Flood Analysis	609
	Witold F. Krajewski, Felipe Quintero, Mohamed El Saadani, and Radoslaw Goska	

33	Global-Scale Evaluation of 22 Precipitation Datasets Using Gauge Observations and Hydrological Modeling	625
	Hylke E. Beck, Noemi Vergopolan, Ming Pan, Vincenzo Levizzani, Albert I. J. M. van Dijk, Graham P. Weedon, Luca Brocca, Florian Pappenberger, George J. Huffman, and Eric F. Wood	
34	OceanRAIN – The Global Ocean Surface-Reference Dataset for Characterization, Validation and Evaluation of the Water Cycle	655
	Christian Klepp, Paul A. Kucera, Jörg Burdanowitz, and Alain Protat	
Part V Observed Characteristics of Precipitation		
35	GPCP and the Global Characteristics of Precipitation	677
	Robert F. Adler, Guojun Gu, George J. Huffman, Mathew R. P. Sapiano, and Jian-Jian Wang	
36	Global Snowfall Detection and Measurement	699
	Mark S. Kulie, Lisa Milani, Norman B. Wood, and Tristan S. L’Ecuyer	
37	Snowfall Detection by Spaceborne Radars	717
	Atsushi Hamada, Toshio Iguchi, and Yukari N. Takayabu	
38	On the Duration and Life Cycle of Precipitation Systems in the Tropics	729
	Rémy Roca, Dominique Bouniol, and Thomas Fiolleau	
39	Observational Characteristics of Warm-Type Heavy Rainfall	745
	Byung-Ju Sohn, Geun-Hyeok Ryu, and Hwan-Jin Song	
40	Satellite Precipitation Measurement and Extreme Rainfall	761
	Olivier P. Prat and Brian R. Nelson	
41	Rainfall Trends in East Africa from an Ensemble of IR-Based Satellite Products	791
	Elsa Cattani, Andrés Merino, and Vincenzo Levizzani	
42	Heavy Precipitation Systems in the Mediterranean Area: The Role of GPM	819
	Giulia Panegrossi, Anna Cinzia Marra, Paolo Sanò, Luca Baldini, Daniele Casella, and Federico Porcù	
43	Dryland Precipitation Climatology from Satellite Observations	843
	Efrat Morin, Francesco Marra, and Moshe Armon	
44	Hailfall Detection	861
	Ralph R. Ferraro, Daniel Cecil, and Sante Laviola	
45	Improving High-Latitude and Cold Region Precipitation Analysis	881
	Ali Behrangi	

46 Latent Heating Retrievals from Satellite Observations 897
 Yukari N. Takayabu and Wei-Kuo Tao

Part VI Applications

47 Operational Applications of Global Precipitation Measurement Observations 919
 Anita LeRoy, Emily Berndt, Andrew Molthan, Bradley Zavadsky, Matthew Smith, Frank LaFontaine, Kevin McGrath, and Kevin Fuell

48 Assimilation of Precipitation Observations from Space into Numerical Weather Prediction (NWP) 941
 Sid-Ahmed Boukabara, Erin Jones, Alan Geer, Masahiro Kazumori, Kevin Garrett, and Eric Maddy

49 Precipitation Ensemble Data Assimilation in NWP Models 983
 Takemasa Miyoshi, Shunji Kotsuki, Koji Terasaki, Shigenori Otsuka, Guo-Yuan Lien, Hisashi Yashiro, Hirofumi Tomita, Masaki Satoh, and Eugenia Kalnay

50 PERSIANN-CDR for Hydrology and Hydro-climatic Applications 993
 Phu Nguyen, Hamed Ashouri, Mohammed Ombadi, Negin Hayatbini, Kuo-Lin Hsu, and Soroosh Sorooshian

51 Soil Moisture and Precipitation: The SM2RAIN Algorithm for Rainfall Retrieval from Satellite Soil Moisture 1013
 Luca Ciabatta, Stefania Camici, Christian Massari, Paolo Filippucci, Sebastian Hahn, Wolfgang Wagner, and Luca Brocca

52 Drought Risk Management Using Satellite-Based Rainfall Estimates 1029
 Elena Tarnavsky and Rogerio Bonifacio

53 Two Decades of Urban Hydroclimatological Studies Have Yielded Discovery and Societal Benefits 1055
 J. Marshall Shepherd, Steven J. Burian, Menglin Jin, Chuntao Liu, and Bradford Johnson

54 Validation of Climate Models 1073
 Francisco J. Tapiador

55 Extreme Precipitation in the Himalayan Landslide Hotspot 1087
 Thomas Stanley, Dalia B. Kirschbaum, Salvatore Pascale, and Sarah Kapnick

56 The Value of Satellite Rainfall Estimates in Agriculture and Food Security 1113
 Tufa Dinku

**57 Using Satellite Estimates of Precipitation for Fire
Danger Rating 1131**
Robert D. Field

58 Variability of Satellite Sea Surface Salinity Under Rainfall 1155
Alexandre Supply, Jacqueline Boutin, Gilles Reverdin,
Jean-Luc Vergely, and Hugo Bellenger

Contents of Volume 1

Part I Status of Observations and Satellite Programs

1	The Global Precipitation Measurement (GPM) Mission	3
	Christopher Kidd, Yukari N. Takayabu, Gail M. Skofronick-Jackson, George J. Huffman, Scott A. Braun, Takuji Kubota, and F. Joseph Turk	
2	Status of the CloudSat Mission	25
	Matthew D. Lebsock, Tristan S. L’Ecuyer, Norman B. Wood, John M. Haynes, and Mark A. Smalley	
3	The Megha-Tropiques Mission After Seven Years in Space	45
	Rémy Roca, Michel Dejus, Philippe Chambon, Sophie Cloché, and Michel Capderou	
4	Microwave Sensors, Imagers and Sounders	63
	Kazumasa Aonashi and Ralph R. Ferraro	
5	Microwave and Sub-mm Wave Sensors: A European Perspective	83
	Christophe Accadia, Vinia Mattioli, Paolo Colucci, Peter Schlüssel, Salvatore D’Addio, Ulf Klein, Tobias Wehr, and Craig Donlon	
6	Plans for Future Missions	99
	Christian D. Kummerow, Simone Tanelli, Nobuhiro Takahashi, Kinji Furukawa, Marian Klein, and Vincenzo Levizzani	

Part II Retrieval Techniques, Algorithms and Sensors

7	Introduction to Passive Microwave Retrieval Methods	123
	Christian D. Kummerow	

8 The Goddard Profiling (GPROF) Precipitation Retrieval Algorithm 141
 David L. Randel, Christian D. Kummerow, and Sarah Ringerud

9 Precipitation Estimation from the Microwave Integrated Retrieval System (MiRS) 153
 Christopher Grassotti, Shuyan Liu, Quanhua Liu, Sid-Ahmed Boukabara, Kevin Garrett, Flavio Iturbide-Sanchez, and Ryan Honeyager

10 Introduction to Radar Rain Retrieval Methods 169
 Toshio Iguchi and Ziad S. Haddad

11 Dual-Frequency Precipitation Radar (DPR) on the Global Precipitation Measurement (GPM) Mission’s Core Observatory 183
 Toshio Iguchi

12 DPR Dual-Frequency Precipitation Classification 193
 V. Chandrasekar and Minda Le

13 Triple-Frequency Radar Retrievals 211
 Alessandro Battaglia, Simone Tanelli, Frederic Tridon, Stefan Kneifel, Jussi Leinonen, and Pavlos Kollias

14 Precipitation Retrievals from Satellite Combined Radar and Radiometer Observations 231
 Mircea Grecu and William S. Olson

15 Scattering of Hydrometeors 249
 Stefan Kneifel, Jussi Leinonen, Jani Tyynelä, Davide Ori, and Alessandro Battaglia

16 Radar Snowfall Measurement 277
 Guosheng Liu

17 A 1DVAR-Based Snowfall Rate Algorithm for Passive Microwave Radiometers 297
 Huan Meng, Cezar Kongoli, and Ralph R. Ferraro

18 X-Band Synthetic Aperture Radar Methods 315
 Saverio Mori, Frank S. Marzano, and Nazzareno Pierdicca

Part III Merged Precipitation Products

19 Integrated Multi-satellite Retrievals for the Global Precipitation Measurement (GPM) Mission (IMERG) 343
 George J. Huffman, David T. Bolvin, Dan Braithwaite, Kuo-Lin Hsu, Robert J. Joyce, Christopher Kidd, Eric J. Nelkin, Soroosh Sorooshian, Erich F. Stocker, Jackson Tan, David B. Wolff, and Pingping Xie

20 Global Satellite Mapping of Precipitation (GSMaP) Products in the GPM Era 355
Takuji Kubota, Kazumasa Aonashi, Tomoo Ushio, Shoichi Shige, Yukari N. Takayabu, Misako Kachi, Yoriko Arai, Tomoko Tashima, Takeshi Masaki, Nozomi Kawamoto, Tomoaki Mega, Munehisa K. Yamamoto, Atsushi Hamada, Moeka Yamaji, Guosheng Liu, and Riko Oki

21 Improving PERSIANN-CCS Using Passive Microwave Rainfall Estimation 375
Kuo-Lin Hsu, Negar Karbalee, and Dan Braithwaite

22 TAMSAT 393
Ross Maidment, Emily Black, Helen Greatrex, and Matthew Young

23 Algorithm and Data Improvements for Version 2.1 of the Climate Hazards Center’s InfraRed Precipitation with Stations Data Set 409
Chris Funk, Pete Peterson, Martin Landsfeld, Frank Davenport, Andreas Becker, Udo Schneider, Diego Pedreros, Amy McNally, Kristi Arsenault, Laura Harrison, and Shraddhanand Shukla

24 Merging the Infrared Fleet and the Microwave Constellation for Tropical Hydrometeorology (TAPEER) and Global Climate Monitoring (GIRAFE) Applications 429
Rémy Roca, Adrien Guérou, Rômulo A. Jucá Oliveira, Philippe Chambon, Marielle Gosset, Sophie Cloché, and Marc Schröder

List of Figures

Fig. 25.1	Distribution of past and current IPWG validation regions and their surface reference data sets	457
Fig. 25.2	Example of IPWG validation over South Africa for gauge data vs the WRF model output on 14 July 2018	458
Fig. 25.3	Example of the IPWG validation of the CMORPH product over the United States, utilising both surface gauge and radar data. The comparison of the gauge and radar provides a useful measure of the retrieval ability of the surface reference data sets	459
Fig. 25.4	Time series of spatial correlation over Japan between the Japan Meteorological Agency (JMA) gauge-calibrated radar data and various satellite estimates and numerical model short-range prediction over the period 1 January 2011 to 31 December 2014. The time series is displayed as an 11-day running mean to improve clarity	461
Fig. 25.5	Temporal correlation over Japan between the JMA gauge-calibrated radar data and various satellite estimates and numerical model short-range prediction for the December–February period during 2011–2014	462
Fig. 25.6	Example of longer-term analysis of precipitation products over Northern Brazil of the IPWG South America validation site. The upper right plot shows the daily gauge-observed precipitation (blue) together with the bias of the GSMaP and TMPA products for 27 December 2014 through 18 August 2016. The lower left plot shows the range of the RMSE for each satellite precipitation product, while the lower right plot shows the bias for the same products	463
Fig. 25.7	Example of instantaneous, full retrieval resolution validation of the GMI precipitation product (GPROF Level 2 version 5) over the European IPWG validation region for 26 January 2016 at 0834 UTC	466

Fig. 26.1 Translation of high-quality precipitation measurements to satellite footprint and swath measurement scales for direct and physical validation 473

Fig. 26.2 VN verification of DPR calibration adjustment. The DPR Ku-band radar calibration was adjusted by JAXA from Version 4 (V4; left) to Version 5 (V5; right). The V5 increase of DPR Ku-Band radar reflectivity (Z_e) by ~ 1.2 dB (y-axis) is clearly evident in relative frequency histograms (shaded, percent) when plotted against the Ku-adjusted VN Z_e (Ground Radar, GR: X-axis) 480

Fig. 26.3 Same as Fig. 26.1, but D_m (mm). Displayed are the V4 (left) and V5 (right) DPR D_m relative to GV. Adjusting the DPR calibration in V5 resulted in a slight, but perceptible positive bias shift in the DPR D_m relative to GV. NASA LISRs for D_m (± 0.5 mm) indicated by dashed lines 480

Fig. 26.4 DPR Measured (left) and PIA-corrected (right) V5 Ku-Band radar reflectivity (y-axis) in convective precipitation plotted against VN radar reflectivity (x-axis) for layers of precipitation below the height of the 0°C level. Similar results are attained for stratiform precipitation (not shown) 481

Fig. 26.5 Coincident and DPR footprint-matched VN-estimated SWER using the Marquette, Michigan WSR-88D radar (KMQT) and Pluvio network in the DPR swath, 15 Apr. 2018. The DPR single frequency estimate (left) is compared against the DP radar (center) and PQPE median estimators (right). The MQT Pluvio network is located west through south of KMQT and within 15 km range. Range rings are illustrated at 50 and 100 km from KMQT 482

Fig. 26.6 Scatter density plots for winter 2017/18 DPR normal swath (y-axis) SWER plotted against VN-estimated SWER (x-axis) for the PQPE 25th% (left), dual-pol (center), and 50th% (right) SWER estimators. It is clear that the DPR SWER estimate best matches the VN dual-polarimetric SWER 482

Fig. 26.7 Evolution of GPM versions. Joint histograms of GV-MRMS reference rain rate (x-axis) for all rain types plotted against matched DPR 2AKu-algorithm IVOV rain rate estimates (y-axis) V04 (left), V05 (center) and V06 (right) 483

Fig. 26.8 Same as Fig. 26.7, but matched-swath dual-frequency combined radar-radiometer algorithm 483

Fig. 26.9 Same as Fig. 26.8, but V5 combined algorithm for stratiform (left) and convective (right) precipitation. The KuPR algorithm strongly resembles this plot as well 484

Fig. 26.10 KuPR (top left) and GMI-GPROF (top right) 50 km gridded mean rate rates (mm h^{-1}) plotted against their matched sample of GV-MRMS (indicated as “Q3”) rain rates in bottom panels 485

Fig. 26.11 GPM V6 combined radar-radiometer algorithm matched-swath rain rates (x-axis) vs. normalized error (%; y-axis) at 50 km grid scales over the CONUS LISR region. Solid line is relative bias, dashed line is NMAE. Green shading represents LISR requirement (Skofronick-Jackson et al. 2018 for V5 result) 486

Fig. 26.12 Similar to Fig. 26.11 (i.e., V6) but for instrument footprint scales in the Kwajalein (K-pol; left), and PAIH (right) oceanic domains. The red line represents bias (%) and the blue line indicates normalized mean absolute error (NMAE; %) at EFOV scales. The solid black line indicates the RMSE (%) for EFOVs scaled to 50 km using Steiner et al. (2003) 487

Fig. 26.13 March 2014 to October 2017 V5b IMERG vs. RAD-RAR statistics for Early (IMERG_E), Late (IMERG_L), Final without gauge adjustment (IMERG_F_U), and Final with gauge adjustment (IMERG_F_G). Top panels: Pearson correlation coefficient (Correlation), Bias (%), NMAE, and NRMSE. Bottom: contingency scores for hits (green), misses (light blue), false alarms (purple), and correct negatives (black). POD, FAR and HSS are also indicated 492

Fig. 26.14 Difference in daily rainfall between RAD-RAR and IMERG-E, L, F-U and F-C, products 492

Fig. 26.15 Error components of IMERG-F V5b Final for March 2014–October 2017 broken down by total bias (E), hit bias (H), biases due to missing precipitation (M), and false precipitation (F) 493

Fig. 26.16 CONUS-wide comparisons of V04A (left) and V5b (right) IMERG-L 30 min rain rates to GV-MRMS for the year of 2015 494

Fig. 26.17 Same as Fig. 26.14, but CONUS IMERG-L compared to GV-MRMS June 2014–August 2017 494

Fig. 26.18 Hurricane Florence total rain accumulation (mm) for 10–16 September 2018. Totals for the GV-MRMS, IMERG-L, and the difference in accumulation between the two (MRMS-IMERG) are displayed in the left, center and right panels, respectively. The location of the maximum accumulations for GV-MRMS and IMERG are indicated by the dark circle 495

Fig. 26.19 Same as Fig. 26.6 and Fig. 26.7, but 30 min rainrates for domain of Fig. 26.16 for IMERG “Precipcal” (left), HQPrecip (microwave; center), and IR (right) during Hurricane Florence 495

Fig. 27.1	Schematic illustration of the measured radar reflectivity profiles by the dual Ka-band radar system. Z_{m1} and Z_{m2} are measured radar reflectivity factors and r is the range	507
Fig. 27.2	Scatter plots of k and Z_e for snow events in 2012. Each figure is with different surface air temperature. Black dots are 1 min data, and dark lines and crosses are fitting curves and averaged values. (Adapted from Nishikawa et al. 2015)	508
Fig. 27.3	The area of comparison over Japan. 0.5° longitude/latitude boxes were set and the entire area was divided into six climatic sub areas considering the total amount of precipitation and near surface air temperature	509
Fig. 27.4	The differences between DPR and AMeDAS rain gauge in six sub areas. Despite slight differences from region to region, the results meet the success criterion that the difference is within $\pm 10\%$ in all cases	511
Fig. 27.5	The area of comparison over the US. The area includes total of 871 1° latitude/longitude boxes	511
Fig. 27.6	The difference between DPR product and MRMS/NMQ by 24 1° latitude bins. The results meet the success criterion of difference within $\pm 10\%$ in 22 bins among 24 bins	512
Fig. 27.7	The rain/snow distribution by JMA's visual reports and DPR data for the case of 18 January 2016 (0900 JST) over north-east part of Japan. The agreement is quite good	513
Fig. 28.1	Map showing the distance to nearest GPCC gauge, typical of all regular and reliable gauge measurements; blank areas in the figure are beyond 100 km from the nearest gauge. (Adapted from Kidd et al. 2017)	522
Fig. 28.2	Global correlation of the 3B42RT (a), CMORPH (b), SM2RAIN (c) and ERA-Interim (d) products obtained by TCA using Triplet A (ERA-Interim-SM2RAIN-3B42RT) for 3B42RT, ERA-Interim and SM2RAIN and Triplet B (ERA-Interim-SM2RAIN-CMORPH) for CMORPH. (Adapted from Massari et al. 2017)	523
Fig. 29.1	MRMS radar quality index. The quality index considers the distance to the closest radar and the beam blockage by the relief (see Zhang et al. 2016 for the definition of the quality index)	536

Fig. 29.2 (a) MRMS hourly precipitation over South-Eastern US, on 30 Nov. 2016 from 0400 to 0500 UTC. (b) Corresponding IMERG hourly precipitation. (c) IMERG error relative to MRMS. (d) Wavelet energy spectra of MRMS (thick black line with circles), IMERG (thick blue line with triangles) and of the error IMERG-MRMS (dashed red line with crosses). The energy spectra are normalised by the total energy (sum of squared values) of the MRMS field 540

Fig. 29.3 Seasonal cumulative precipitation from Nov. 2016 to Apr. 2017 (cold season) and May – Oct. 2017 (warm season) for MRMS and IMERG. The fields are spatially smoothed through sliding window averaging with a 640 km wide window (corresponding to the smoothing function associated with the Haar wavelet) 541

Fig. 29.4 Average wavelet energy spectra of MRMS (black line with circles), and IMERG (blue line with triangles) hourly precipitation fields and of the error IMERG-MRMS (dashed red line with crosses), computed over CONUS Nov. 2016 – Apr. 2017 (cold season) and May – Oct. 2017 (warm season). The spectra are computed at each time step and summed over the analysed period. The energy spectra are normalised by the total energy (sum of squared values) of the MRMS fields. Only the pixels with a MRMS radar quality index >0.9 are retained for the computation of the spectra 542

Fig. 29.5 Ratio of the spectral energy of IMERG hourly precipitation fields over the spectral energy of MRMS hourly precipitation fields during the cold and warm seasons. The spectral energies are computed at each time step and summed. A ratio close to one at all scales indicates the agreement of the IMERG and MRMS wavelet energy spectra 544

Fig. 29.6 Ratio of the spectral energy the IMERG hourly error (i.e., IMERG-MRMS) over the spectral energy of MRMS hourly precipitation during the cold and warm seasons. The spectral energies are computed at each time step and summed. A low spectral energy of the error indicates the agreement between IMERG and MRMS spatial patterns (gradients) at the corresponding scale 546

Fig. 29.7 Linear correlation between the wavelet coefficients of the IMERG and MRMS hourly precipitation fields. A high correlation of the wavelet coefficients indicates the agreement between IMERG and MRMS spatial patterns (gradients) at the corresponding scale. Contrary the spectral energy of the error, the correlation is not sensitive to potential biases in the magnitude of the wavelet coefficients 548

Fig. 29.8 Effective resolution of IMERG hourly precipitation evaluated against MRMS during the cold and warm seasons. The criterion (29.3) is used to define the effective resolution 550

Fig. 29.9 Same as Fig. 29.4 for the cold season, but computed only over the South-Eastern region where the effective resolution is found finer than 160 km 551

Fig. 29.10 Effective resolution of IMERG daily precipitation evaluated against MRMS during the cold and warm seasons. The criterion (29.3) is used to define the effective resolution 552

Fig. 29.11 Representation of the spatial convolution filters used to perform the two-dimensional Haar wavelet decomposition. A and B and C are the wavelet functions ψ^H , ψ^V and ψ^D used to compute the horizontal (HL), vertical (LH) and diagonal (HH) wavelet coefficients. D is the smoothing function ϕ^{2D} used to compute the smoothing (LL) coefficients. The four functions are orthogonal, meaning that the scalar product of one with any of the other three equals zero 555

Fig. 29.12 Illustration of the discrete wavelet decomposition process of a two-dimensional field (using the Haar wavelet) 555

Fig. 30.1 Histogram of daily rainfall observed along an altitudinal rain gauge transect on the eastern slopes of the Peruvian Andes (Barros 2013). Stations with incomplete records were removed. A, B, C refer to different pixels of TRMM 3B42 and GPM IMERG products. The red (tropical montane forest) and orange (cloud forest) lines represent the rainfall envelope for the two main ecosystems 561

Fig. 30.2 Conceptual representation of orographic precipitation mechanisms in the Southern Appalachian Mountains. (Adapted and modified from Wilson and Barros 2017) 562

Fig. 30.3 Example of ground-clutter effects on radar measurements of low-level rainfall. Left: Vertical structure of MRR reflectivity above ground level (AGL) with GPM overpass marked by the pink dashed line in right panel. Right: Reflectivity cross-section over the Southern Appalachian Mountains. Black dashed lines indicate the boundaries of near-nadir scan (angle <7 deg). Pink line marks the position of the MRR where rainfall was missed by the GPM DPR algorithm. The white band between the terrain (dark black line) and the GPM reflectivity lower reflectivity measurements (red band) is due to the terrain mask used in the algorithm 565

Fig. 30.4 Dependence of detection errors to the satellite orientation. Detection errors varying with **(a)** satellite geometry and **(b)** local viewing angle. Near-surface precipitation estimates of Level 2, version 5A products of GPM Ku-PR compared with ground-based rain-gauges (RG) that lie within 2.5 km of the center of DPR pixels. Time period considered for analysis: March 2014–May 2017. Note- YY is when both GPM and RG detects precipitation. FA is false alarm when GPM detects precipitation while RG did not detect any precipitation. MD is missed detection where RG detects rain and GPM misses the detection 566

Fig. 30.5 Location of IPHEX GV (left) rain-gauges and (right) Parsivel disdrometers in the SAM. Triangles denote ridge (elevation >900 m) and circles denote valley locations 567

Fig. 30.6 Spatial distributions of AQUA MODIS LLCF (CTH <5 MSL, confident cloudy only; 0.05° × 0.05°) during daytime (Left Column) and nighttime (Right Column) overpasses in summer (June–July–August; top row) and winter (December–January–February; bottom row). (Adapted from Duan and Barros 2017) 568

Fig. 30.7 Fingerprinting SFI on DSD metrics. Left: diurnal cycle of Dm (ratio of fourth moment to the third moment of the diameter) at P4 (western ridge) and P6 (foothills). Right: diurnal cycle of rain and fog occurrences at P4. Note that Dm (P6) always ≥ Dm (P4). FCC: Fog and Cap Clouds. LLC: Layered Low Level Clouds 569

Fig. 30.8 Left: diurnal cycle of GPM revisit overpasses over the region shown in Fig. 30.5. Right: Spatial distribution of rainfall detection. The blue tones in the inner region valleys and over the complex terrain at low elevations along the eastern ridges of the SAM are indicative of low frequency bias 570

Fig. 30.9 DSD nonstationarity on altitudinal gradients: **(a)** disdrometer (continuous lines) and GPM Ku-PR estimates (dashed lines) on the western slopes of the SAM; **(b)** and **(c)** DSD statistics on the eastern slopes of the SAM 570

Fig. 30.10 **(a)** Seasonal and **(b)** diurnal distribution of GPM Ku-PR detection errors in the Southern Appalachian Mountains for ascending and descending modes of the GPM 570

Fig. 30.11 **(a)** Detection and **(b)** estimation errors varying with rain-gauge rain-rate observations for ascending and descending modes of the GPM Ku-PR. $Bias = 10\log_{10}\left(\frac{\sum R_{GPM,i}}{\sum R_{RG,i}}\right)$ 571

Fig. 30.12 Average GPM Ku-PR Level 2A DSD parameters in the SAM for 4.5 years since GPM launch. Top row: spatial distribution of (a) D_m and (b) N_w . Bottom row: vertical structure along the transect at $83.5^\circ W$ (black line in b) of (c) N_w and (d) D_m . The pink circles and triangles mark respectively valley and ridge disdrometer locations 572

Fig. 30.13 Phase-space maps of (D_m , N_w) from GPM Level 2A products since launch and from GV Parsivel disdrometer P18 during IPHEX 573

Fig. 30.14 Left: sensitivity analysis of surface rainfall accumulation to the drop size distribution (DSD) spectra of fog in the simulation of RoF SFI at P6 in the western foothills of the SAM. RG-dashed black lines are local raingauge observations. After Duan and Barros (2017). Right: simulated microphysical trajectory for stratiform rainfall with and without RoF SFI at P6 corresponding to Fog#4 DSD and fog depth of 400 m. Circles describe microphysical state at 1-min intervals from start to end of the event as per the legend 574

Fig. 30.15 Composites of GPM Level 2A DSD parameters and reflectivity along a cross-section designed to capture the hot-spots of precipitation in Central Himalayas ($84.4^\circ E$, red circle) during the monsoon. Orographic precipitation on the upwind slopes is highlighted by the boxes. The map with TRMM Precipitation Features (PFs) on the left panel is adapted from Barros et al. (2004) 574

Fig. 30.16 Left panels: diurnal cycle of the spatial distribution of the climatology of Probability of Detection (PoD) of IMERG precipitation (~ 11 km spatial resolution) compared with STAGE IV (~ 4 km spatial resolution) (<http://www.emc.ncep.noaa.gov/mmb/ylin/pcpanl/stage4/>, last accessed 4 Dec. 2018). Time period of analysis- March 2014 to February 2017. Right panels: diurnal cycle of Parsivel disdrometer DSD measurements at locations marked in the left panel 575

Fig. 30.17 Illustrative sketching of typical DSD evolution in the lower troposphere under when different Seeder-Feeder Interactions (SFI) scenarios. *ABGL* Above Ground Level, *D* Diameter, *N(D)* number concentration 577

Fig. 30.18 Contour frequency by altitude synthesis of reflectivity profiles derived from Weather Research Forecast (WRF) model V3.8 simulations using the standard continental aerosol in the model (left) and using aerosol properties measured in Central Nepal. Details of the simulation can be found in Barros et al. (2018) 577

Fig. 31.1 Research framework and overview flowchart to bridge from the Global Precipitation Measurement mission core satellite to the combined gridded IMERG product using ground radar-based Multi-Radar/Multi-Sensor QPE. An example of Multi-Radar/Multi-Sensor instantaneous precipitation rates at 0725 UTC on 11 April 2011 is shown 585

Fig. 31.2 Comparison framework across Level-2 and Level-3 satellite QPE to bridge from the GPM core satellite to IMERG 594

Fig. 31.3 Reference (a) and DPR (b) rainfall rate distributions (mm h^{-1}) as functions of the CPI (%). The thick black line represents the median (50% quantile), the dark grey-shaded region represents the area between the 25 and 75% quantiles, the light grey-shaded region represents the area between the 10 and 90% quantiles 595

Fig. 31.4 DPR residual distributions (mm h^{-1}) as functions of the CPI (%). The thick black line represents the median (50% quantile), the dark grey-shaded region represents the area between the 25 and 75% quantiles, the light grey-shaded region represents the area between the 10 and 90% quantiles 596

Fig. 31.5 Conditional bias of spaceborne radars relative to the reference as a function of the CPI (%) for the GPM-DPR/Ku (black), GPM-DPR/Ka (blue), GPM-DPR/Ka-Ku (red) and TRMM-PR (grey) 597

Fig. 31.6 Reference and GPROF-GMI cumulative distribution of convective contribution 598

Fig. 31.7 GPROF-GMI residual distributions (mm h^{-1}) as functions of the CPI (%). The thick black line represents the median (50% quantile), the dark grey-shaded region represents the area between the 25% and 75% quantiles, the light grey-shaded region represents the area between the 10% and 90% quantiles 599

Fig. 31.8 GPROF-GMI (left) systematic part –conditional median - and (right) random part –interquantile 10%–90%- of error 599

Fig. 31.9 GPROF-GMI (left) correlation and (right) relative bias as a function of convective contribution difference between GPROF-GMI and the reference 600

Fig. 31.10 IMERG residual distributions (mm h^{-1}) as functions of the CPI (%). The thick black line represents the median (50% quantile), the dark grey-shaded region represents the area between the 25 and 75% quantiles, the light grey-shaded region represents the area between the 10 and 90% quantiles 601

Fig. 31.11 IMERG (left) systematic part – conditional median – and (right) random part – interquantile 10–90% – of error for the PMW component (red) and IR component (blue) 602

Fig. 32.1 Correlation coefficient between hydrologic model prediction and streamflow observations at 130 gauges in Iowa. The IMERG forced model results are on the left, the MRMS-forced model output is on the right 612

Fig. 32.2 Northeast Iowa, the site of the 2013 Iowa Flood Studies field campaign. The outlined river basins include Turkey River, Cedar River and Iowa River 614

Fig. 32.3 The width function for the Cedar River basin with the outlet at Cedar Rapids, Iowa. In constructing the plot, we assumed a constant stream velocity of 0.75 m s^{-1} . It is clear that the streams that are located 200–400 km from the outlet, contribute most to the discharge 614

Fig. 32.4 The panels on the left correspond to the gridded representation of rainfall for radar-based (top) and satellite-based (middle) products and the difference (bottom). On the right, we show the same rainfall but calculated for the areas upstream from a given link of the river network for several watersheds in northeast Iowa 616

Fig. 32.5 Panel (a) shows network integrated rainfall difference between a reference and a product of interest. Panel (b) shows the differences in the peak flow for all streams in the network based on a simple linear model; panel (c) shows the same but for a nonlinear model 617

Fig. 32.6 Network-integrated rainfall for the reference product (MRMS) and a satellite product (IMERG). The third panel show the relative differences between the two products 619

Fig. 32.7 Standard deviation (in mm) of the rainfall product discrepancies calculated in Euclidean space (black), and over the river network for flow-connected segments (red) and flow-unconnected segments. The inset illustrates the flow-connected and unconnected cases 620

Fig. 33.1 For a selection of the evaluated uncorrected P datasets, temporal correlations between 3-day mean gauge- and dataset-based P time series ($R_{3\text{day}}$). Each data point represents a gauge. See Beck et al. (2017c) for global maps of the other performance metrics 636

Fig. 33.2 Calibration NSE scores obtained using P time series from (a) CHIRPS V2.0, (b) CMORPH-CRT V1.0, (c) CPC Unified, (d) MSWEP V1.2, (e) MSWEP V2.0, (f) PERSIANN-CDR V1R1, (g) TMPA 3B42 V7, and (h) WFDEI-CRU. Each data point represents a catchment centroid. Only the eight best performing P datasets are shown 641

Fig. 33.3 For each catchment, the P dataset with the highest calibration NSE. Each data point represents a catchment centroid. Only the seven best performing P datasets (excluding MSWEP V1.2 due to its similarity to V2.0) are considered. Note that CHIRPS V2.0, CMORPH-CRT V1.0, PERSIANN-CDR V1R1, and TMPA 3B42 V7 do not provide data beyond 50, 60, 60, and 50° latitude, respectively 642

Fig. 34.1 OceanRAIN shipboard data ingest and post-processing flow chart. (Adapted from Klepp et al. 2018) 660

Fig. 34.2 OceanRAIN data distribution for all eight ships (a), seasons (b), years (c) and precipitation occurrence for type (rain, snow, mixed) and true-zeros (d). (Adapted from Klepp et al. 2018) 662

Fig. 34.3 Latitudinal fraction of the precipitation phase with red for rain, blue for snow and green for mixed phase (a). The scatter diagram shows individual precipitation minutes for phases against latitude as a function of precipitation rate (mm h^{-1}). Panels (b) shows the joint histogram of the precipitation rate in mm h^{-1} and the orange line indicates bin-wise mean for 2° latitude bands. Frequency of occurrence in % of all cases is shown with colors. Panel (c) shows the Rayleigh reflectivity log (Z) and log (R) distribution of rainfall for all 696,740 events (black), 139,557 stratiform events (blue) and 15,823 convective events (red). Panel (d) denotes the mean number concentration PSDs (thick marks) and their latitudinal variability (thin marks) for all rainfall (red), snowfall (blue) and mixed-phase precipitation (green). (Adapted from Klepp et al. 2018) 665

Fig. 34.4 Maps of average precipitation-rate difference of HOAPS (R_H) subtracted by adjusted OceanRAIN ($R_{O^{**}}$) in mm h^{-1} per 2° × 2° grid-box for (a) hits, (b) misses, (c) false detections and d) all cases. Gray boxes have no data available. (e) Map of occurrence of precipitation from 24,990 HOAPS–OceanRAIN collocations from available long-term RVs in OceanRAIN from 06/2010–12/2015 (cyan dots), misses ($R_H = 0$ and $R_{O^{**}} > 0$; purple) and hits ($R_H > 0$ and $R_{O^{**}} > 0$; orange) using ±20 km and ± 30 min as collocation boundaries. (Adapted from Burdanowitz et al. 2018) 667

Fig. 34.5 Location of matched OceanRAIN-IMERG pairs for the period 20 March 2014–28 February 2017. The “x” symbol indicates rain events, and “+” symbol indicates snow events. Ship tracks of OceanRAIN database. R/V Investigator (red), R/V Merian (magenta), R/V Meteor (blue), R/V Polarstern (cyan), R/V Revelle (green), R/V Sonne II (yellow), R/V World (black) 669

Fig. 34.6	Scatterplot of matched IMERG and OceanRAIN pairs. The colors indicate the ship that observed the precipitation. The “+” symbol indicates rain pairs and “×” symbol indicates snow pairs	670
Fig. 34.7	Plot of cross-correlation of rainfall for neighboring IMERG grids	670
Fig. 34.8	Scatter plot of matched pairs for convective and stratiform rainfall	671
Fig. 35.1	GPCP climatological mean precipitation (mm day^{-1}) during 1979–2017	680
Fig. 35.2	Latitudinal profiles of mean zonal precipitation (1979–2017) for land, ocean and combined	680
Fig. 35.3	Seasonal mean GPCP precipitation (mm day^{-1}). (a) December–January–February (DJF), (b) March–April–May (MAM), (c) June–July–August (JJA), and (d) September–October–November (SON)	681
Fig. 35.4	Time series (January 1979–December 2017) of global mean (land+ocean) precipitation (black line), and corresponding ENSO (red) and volcanic effects (blue)	684
Fig. 35.5	Composite precipitation anomaly changes (%) between ENSO warm (defined as Niño 3.4 ≥ 0.34) and cold phases (Niño 3.4 ≤ -0.45). The number of months for either phase is 155 (one third of months) during 1979–2017	686
Fig. 35.6	Long-term trends in (a) GISS surface temperature (ts; 1979–2017), (b) SSMI/SSMIS columnar water vapor (CWV; 1988–2014), and (c) GPCP precipitation (1979–2017). (d) Long-term trend in precipitation without the effect of PDO and AMO	687
Fig. 35.7	Zonal mean precipitation trend during 1979–2017 from GPCP (black curve). Also shown is the zonal mean profile of climatological mean precipitation (red curve; scaled by 50 with resulting units of mm day^{-1}). Green and blue curves are the trend curves for CMIP and AMIP climate model ensembles for similar periods	689
Fig. 35.8	Long-term trends (mm day^{-1} per decade) in (a) GPCP precipitation (1979–2017), (b) GPCP precipitation with no PDO effect, (c) AMIP precipitation (1979–2008), and (d) CMIP5 historical full forcing precipitation (1979–2012)	690